Large eddy simulation of flow and scalar transport in a vegetated channel

Noname manuscript No.
(will be inserted by the editor)

Large eddy simulation of flow and scalar transport in a vegetated channel

Chao Yan · Heidi M. Nepf · Wei-Xi Huang · Gui-Xiang Cui

Received: date / Accepted: date

Abstract Predicting flow and mass transport in vegetated regions has a broad range of applications in ecology and engineering practice. This paper presents large eddy simulation (LES) of turbulent flow and scalar transport within a fully developed open-channel with submerged vegetation. To properly represent the scalar transport, an additional diffusivity was introduced within the canopy to account for the contribution of stem wakes, which were not resolved by the LES, to turbulent diffusion. The LES produced good agreement with the velocity and concentration fields measured in a flume experiment. The simulation revealed a secondary flow distributed symmetrically about the channel centerline, which differed significantly from the circulation in a bare channel. The secondary circulation accelerated the vertical spread of the plume both within and above the canopy layer. Quadrant analysis was used to identify the form and shape of canopy-scale turbulent structures within and above the vegetation canopy. Within the canopy, sweep events contributed more to momentum transfer than ejection events, whereas the opposite occurred above the canopy. The coherent structures were similar to those observed in terrestrial canopies, but smaller in scale due to the constraint of the water surface.

The work was supported by National Natural Science Foundation of China under Grants No. 11132005 and 11322221, and by US National Science Foundation Grant No. AGS-1005480. The authors would also like to thank Tsinghua National Laboratory for Information Science and Technology for the support in parallel computing.

Chao Yan · Wei-Xi Huang · Gui-Xiang Cui
Department of Engineering Mechanics, Tsinghua University, Beijing, 100084, China
Tel.: 86-10-62797215
E-mail: hwx@tsinghua.edu.cn

Heidi M. Nepf
Department of Civil and Environmental Engineering, Massachusetts Institute of Technology, Cambridge, Massachusetts, USA
Tel.: 001-617-253-8622
E-mail: hmnepf@mit.edu

Keywords Vegetation canopy · Large eddy simulation · Turbulence structures · Secondary flow · Scalar transport

1 Introduction

Vegetation is a fundamental component of aquatic ecosystems. By removing nutrients from and releasing oxygen to the water column, vegetation improves water quality [1,2]. Vegetation can locally reduce bed shear stress [3], stabilizing the sediment and promoting carbon sequestration [4]. In the coastal zone, seagrasses provide habitat for economically important shellfish, such as clams and mussels [5,6]. Recognizing its positive ecological function, efforts to restore aquatic vegetation have increased [7]. Many of the ecological processes mediated by vegetation involve the transport of scalars. For example, scalar transport between a submerged meadow and surrounding open water may influence the overall rate of nutrient uptake by a meadow, the capture of particulates within a meadow, or the recruitment of larvae to a meadow. The transport of pollen between meadows can increase genetic diversity, which has been shown to enhance meadow recovery after disturbance [8]. Despite the ecological importance of scalar transport in regions of submerged vegetation, only a relatively few studies have examined it [9,10]. Scalar transport within vegetated flows is complex, because it is dependent on processes at several scales, from individual blades to vegetation heterogeneity at the meadow and landscape scales [11]. A deeper understanding of relevant dispersion processes is needed to achieve a complete description of the ecological services provided by vegetation.

The enhanced flow resistance provided by a canopy shapes the velocity profile and the turbulence structure. For a submerged canopy, there are three distinct regions [12]. In the lower canopy, von Karman vortex streets shed by individual plant elements contribute to turbulent diffusion (e.g. Lightbody and Nepf [11]). In the upper canopy and extending some distance above the canopy, there is a mixing-layer within which Kelvin-Helmholtz (KH) vortices dominate the mass and momentum exchange between the canopy and the overflow (e.g. Ghisalberti and Nepf [13,14], Raupach et al. [15]). Finally, if the water depth is sufficient, above the canopy, the mixing layer profile transitions to a turbulent boundary layer (e.g. Nepf and Vivoni [16]).

Numerical simulations have been widely utilized to investigate vegetated channel flows, including direct numerical simulation (DNS), Reynolds-averaged Navier-Stokes (RANS), and large eddy simulation (LES). DNS solves the full Navier-Stokes equations for all scales of fluid motion, but is computationally demanding and only applicable to flow at relatively low Reynolds number. RANS solves only the time-averaged governing equations, with the effects of turbulence accounted for by a turbulence closure. In LES, the large-scale turbulent motions are fully resolved, with the effect of small-scale motions represented by subgrid-scale models. López and García [17] performed RANS simulations of flow through submerged vegetation using a two-equation turbulence closure. They added an extra production term to reflect the stem-scale turbulence produced in the plant wakes. Using the Tanino and Nepf [18] model to represent stem-scale turbulence, King et al. [19] introduced an improved two-equation $k-\varepsilon$ model, which outperformed traditional $k-\varepsilon$ models in predicting turbulent kinetic energy (TKE) within the canopy layer. They suggested that their model could be a foundation for predicting scalar dispersion within dense vegetation canopies, an option that we explore in the current study. Okamoto and Nezu [20] performed LES of a vegetated open-channel flow under six different ratios of water depth to the canopy height. They found that the sweep and ejection motions associated with the KH vortices dominate the momentum and mass transport in the upper canopy, consistent with previous experimental observations [13,14].

The goal of the present work is to further explore the effects of vegetation on flow and scalar transport in a fully-developed channel flow using LES. LES was chosen because, unlike RANS, it can explicitly represent the KH coherent structures that dominate scalar exchange at the top of the canopy [13,14,20]. In addition, flow in a rectangular channel generates secondary circulations that can affect scalar transport [21], and which cannot be reproduced by RANS models that use an isotropic eddy viscosity [22]. Importantly, the LES model used in the current study contains a new turbulent diffusivity term, based on Tanino and Nepf [18], that represents the contribution of stem-generated turbulence to turbulent diffusivity within the canopy. Section 2 describes the numerical and physical models. Section 3 compares the mean flow, turbulence statistics, and scalar concentration fields from the numerical simulations to measured data. Finally, Section 4 provides the conclusions and main findings.

2 The Governing Equations and Numerical Implementation

2.1 Numerical Model and Discretization Method

LES directly solves the larger scales of turbulent motion, called the resolved scales, which are separated from the sub-grid scales by a spatial filter. Application of a spatial filter to the incompressible Navier-Stokes equations yields:

$$\frac{\partial \widetilde{u_i}}{\partial x_i} = 0 \tag{1}$$

$$\frac{\partial \widetilde{u_i}}{\partial t} + \frac{\partial (\widetilde{u_i}\widetilde{u_j})}{\partial x_j} = -\frac{1}{\rho}\left(\frac{\mathrm{d}P^*}{\mathrm{d}x_1}\delta_{i1} + \frac{\partial \widetilde{p}}{\partial x_i}\right) + \frac{\partial}{\partial x_j}\left(\upsilon \frac{\partial \widetilde{u_i}}{\partial x_j} + \tau_{ij}\right) + F_{Di} \tag{2}$$

in which the tilde indicates the filtered variables; ρ (998.2 kg m^{-3}) and υ (1.004 $\times$ 10^{-6} m^2 s^{-1}) are the fluid density and kinematic viscosity, respectively; $\widetilde{u_i}(\widetilde{u_1} = u, \widetilde{u_2} = v, \widetilde{u_3} = w)$ represents the filtered velocity component in the $x_i(x_1 = x, x_2 = y, x_3 = z)$ direction, respectively; $\widetilde{p}$ is the filtered pressure; and $\mathrm{d}P^*/\mathrm{d}x_1$ denotes the externally imposed streamwise pressure gradient that is adjusted at every time step to maintain a constant flow rate. The subgrid-scale

(SGS) stress tensor τ_{ij} is defined below. The body force term F_{Di} represents the drag exerted by vegetation, which is parameterized as the product of the drag coefficient C_D, the frontal area density a, and mean streamwise current speed:

$$F_{Di} = -\frac{1}{2} C_D a |U| \widetilde{u} \tag{3}$$

in which U is the magnitude of the velocity. The passive scalar transport equation is solved as well:

$$\frac{\partial \widetilde{c}}{\partial t} + \frac{\partial (\widetilde{u_i} \widetilde{c})}{\partial x_i} = \frac{\partial}{\partial x_i} \left(\tau_{ci} + \frac{\upsilon}{Sc} \frac{\partial \widetilde{c}}{\partial x_i} + D_t \frac{\partial \widetilde{c}}{\partial x_i} \right) + S \tag{4}$$

in which $\widetilde{c}$ denotes the filtered concentration, S is the scalar source term, τ_{ci} is the SGS scalar flux, and Sc ($= \upsilon/D$) is the Schmidt number. Because the stem-scale turbulence is not resolved by the LES, a turbulent diffusivity D_t is introduced in Eq. (4) to reflect the effect of stem wake turbulence on mass transport. Tanino and Nepf [18] measured stem-wake turbulence and its contribution to turbulent diffusion in a model emergent canopy consisting of rigid circular cylinders of diameter d. For a sparse canopy, as is considered in this study, stem-scale eddies exist throughout the canopy, so that Eqs. (2.12) and (2.15) in Tanino and Nepf [18] reduce to:

$$\sqrt{k_t} = 1.1 U_p \left[C_D \frac{\phi}{(1-\phi)\pi/2} \right]^{1/3} \tag{5}$$

$$D_t = \alpha \sqrt{k_t} d \tag{6}$$

in which U_p is the mean velocity within the canopy, and ϕ is the solid volume fraction occupied by the canopy elements. For lateral diffusivity, Tanino and Nepf [18] reported α equal to 4.5. Within an array of vertical circular cylinders, the diffusivity is anisotropic, with $D_z/D_y \approx 0.26$ for $\phi = 0.05$ (based on data in Nepf et al. [23]), which is comparable to our value (Table 1), so that we estimate $\alpha = 1.2$ for vertical diffusivity.

The subgrid-scale (SGS) stress tensor $\tau_{ij} = \widetilde{u_i} \widetilde{u_j} - \widetilde{u_i u_j}$ captures the effect of the subgrid scales on the resolved scales, and it is modelled in terms of resolved velocity field using the Lagrangian dynamic model, i.e.

$$\tau_{ij} = 2 \upsilon_t \widetilde{S_{ij}} + \frac{1}{3} \tau_{kk} \delta_{ij} \tag{7a}$$

$$\upsilon_t = (C_s \Delta)^2 \sqrt{2 S_{ij} S_{ij}} \tag{7b}$$

in which $\Delta = \sqrt[3]{\Delta x \Delta y \Delta z}$ is the filter width, $\widetilde{S_{ij}} = (\partial \widetilde{u_i}/\partial x_j + \partial \widetilde{u_j}/\partial x_i)/2$ is the resolved strain-rate tensor, υ_t is the SGS eddy viscosity, and C_s is the subgrid model coefficient. The value of C_s is determined dynamically by invoking the Lagrangian dynamic procedure [24], which applies well in predicting flow over both aquatic canopies [25] and terrestrial canopies [26].

The SGS scalar flux $\tau_{ci} = \widetilde{u_i}\widetilde{c} - \widetilde{u_i c}$ is modelled based on the gradient-diffusion hypothesis, which relates the turbulent scalar flux to the mean gradient of the concentration as:

$$\tau_{ci} = \frac{\upsilon_t}{Sc_t}\frac{\partial \widetilde{c}}{\partial x_i} \tag{8}$$

Observations suggest that the turbulent Schmidt number $Sc_t = 0.47$ in canopy flows with shallow submergence [13]. Although experimental results and RANS simulations suggest that an eddy-diffusivity tensor is more appropriate to describe the turbulent diffusion [27,28], previous studies have demonstrated that this standard gradient-diffusion model is valid in the framework of LES when dealing with cases in which the model fails to accurately predict passive scalar transport in RANS [29].

The spatial terms in the Navier-Stokes equations (1) and (2) are discretized using a cell-centered finite volume method (FVM) in semi-discrete form. Time integration is performed by Runge-Kutta scheme with fourth-order temporal accuracy. Further details about the numerical methods and validation can be found in Yan et al. [30]. Henceforth, tilde symbols used to denote resolved variables is ignored to simplify the notation.

2.2 Simulation set-up

The simulation recreates the laboratory experiment described in Ghisalberti and Nepf [13,31], which used a model canopy consisting of circular cylinders of height h = 13.8 cm and diameter d = 0.64 cm, and with canopy density a = 8.0 m^{-1}. Since the roughness density $\lambda = ah = 1.1 \gg 0.1$, this represents a dense canopy [32], for which the shear-layer turbulence could not penetrate to the bed. The canopy extended across the entire flume width (w_f = 38 cm), and the water depth was H = 46.7 cm. The measured drag coefficient was C_D = 0.66 (Ghisalberti and Nepf [31], Table 1). In the experiment of Ghisalberti and Nepf [13], neutrally buoyant dye was continuously injected from twelve needles spaced 3.5 cm apart in the lateral direction at the top of the canopy.

The streamwise length of the computational domain L_x was 4.0 m, chosen to be large enough to encompass a wide range of spatial scales. The computational domain, shown in Fig. 1, was discretized evenly in the streamwise and spanwise directions. The grids were uniformly distributed laterally in order to create a scalar source distribution identical to the experiment. The mesh was locally refined near the bed and at the top of canopy layer to resolve the steep variation in mean flow and turbulence statistics in these regions. Table 1 tabulates the main parameters of the LES.

Periodic boundary conditions were imposed in the streamwise direction to simulate an infinite array, and a frictionless rigid lid condition was used at the water surface. A no-slip boundary condition was applied at the bed and side walls using the Obukhov wall function with a roughness length $z_0 = 0.001h$ [33]. For the scalar modeling, zero-gradient (no-flux) boundary conditions were

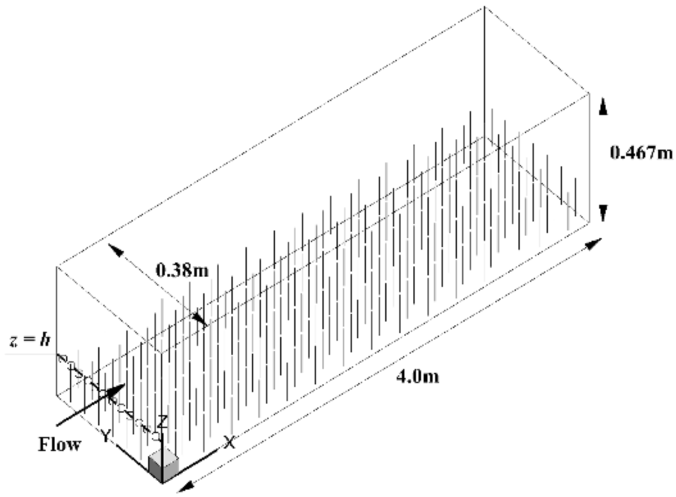

Fig. 1 Schematic of the computation domain and associated coordinate system. Circles indicate the scalar point sources. In the experiment, the canopy consisted of vertical circular cylinders, which are conceptually represented in the figure. However, within the LES, the canopy was represented as a distributed drag and the cylinders were not resolved.

Table 1 Experimental and computational conditions

Case	Canopy height h (cm)	Water depth H (cm)	U_{bulk} (cm s^{-1})	C_D	ϕ	a (m^{-1})	L_x (m)	w_f (cm)
R8	13.8	46.7	5.7	0.66	0.04	8.0	4.0	38.0

applied to the bottom, side walls and free surface, while convective boundary conditions were imposed at the outlet. To examine the effect of the channel aspect ratio, additional simulations were conducted with width-to-height ratios $w_f/H = 2$, 5, 10, and ∞ by varying the width of the channel w_f while maintaining the depth of submergence H/h $(= 3.38)$. The infinitely wide channel was simulated by using spanwise periodic boundary conditions, and the size of the computation domain was the same as the validated case. Note that this range of aspect ratios is consistent with typical values in field-scale open-channels, which can vary from an order of 1 for conveyance canals [34] to an order of 10 or more for fluvial systems [35]. The bulk velocity was the same for all the simulations. For all aspect ratios, the mass injection was created using twelve scalar sources evenly distributed across the channel width at the top of the canopy $(z = h)$, see Fig. 1.

The instantaneous flow quantities, such as velocity component u_i, are decomposed into three components,

$$u_i(x,y,z,t) = \langle \overline{u_i} \rangle (y,z) + u_i'(x,y,z,t) + \overline{u_i}''(x,y,z) \tag{9}$$

in which the overbar denotes a time average, the angle bracket denotes a streamwise average, and the temporal and spatial fluctuations are denoted by a single prime and a double prime, respectively. Applying this double-averaging method to the momentum equation yields the following [36],

$$\frac{\partial(\langle\overline{u_i}\rangle\,\langle\overline{u_j}\rangle)}{\partial x_j} = -\frac{1}{\rho}\left(\frac{\mathrm{d}P^*}{\mathrm{d}x_1}\delta_{i1} + \frac{\partial\langle\overline{p}\rangle}{\partial x_i}\right) + \frac{\partial\chi_{ij}}{\partial x_j} + F_{Di} \tag{10}$$

in which the total shear stress χ_{ij} consists of the spatial average of Reynolds and viscous stresses, together with the dispersive stress due to spatially averaged velocity field differs from local temporal means,

$$\chi_{ij} = -\langle\overline{u_i}''\overline{u_j}''\rangle - \left\langle\overline{u_i{}'u_j{}'}\right\rangle + \upsilon\frac{\partial\langle\overline{u_i}\rangle}{\partial x_j} \tag{11}$$

The velocity moments were extracted at three lateral locations corresponding to the acoustic Doppler velocimetry (ADV) measurements of Ghisalberti and Nepf [13,31], and then averaged to produce vertical profiles of turbulence statistics. For comparison to the experiment, the scalar concentration was extracted at the same six streamwise cross-sections as reported in the experiment.

3 Results and Discussion

3.1 Mean Flow and Turbulence Statistics

In Fig. 2, the vertical profiles of turbulence statistics are compared to experimental data [31]. The simulation using a periodic sidewall condition, which does not generate the secondary circulation, is included in Fig. 2 for comparison. In each subplot, the simulation with no-slip sidewalls and periodic sidewalls are plotted with solid and dashed curves, respectively. The simulated velocity profile agreed well with the measurements, with slightly better agreement from the simulation with no-slip sidewalls (solid line, Fig. 2a). Importantly, the no-slip sidewall simulation correctly captured the reduction of velocity magnitude when approaching the free surface, which is associated with the secondary circulation in the channel, the dynamics of which are discussed in Sect. 3.3. The no-slip sidewall model also predicted the vertical distribution of Reynolds stress (RS) within the canopy and very close to the water surface, specifically capturing the region of $\overline{u'w'} = 0$ near the surface, which is associated with the secondary circulation. The periodic sidewall simulation (dashed line) did not capture the peak RS or the region of $\overline{u'w'} = 0$ near the surface. Both simulations underpredicted the near-bed velocity, which was likely due to the choice of z_0, which was not calibrated. The predicted turbulent kinetic energy (TKE) obtained by both simulations with the additional stem-scale TKE Eq.(5) was in good agreement with experimental measurements, especially within the canopy layer, indicating that the addition of Eq.(5) correctly accounted for the missing stem-scale TKE in the canopy. To better

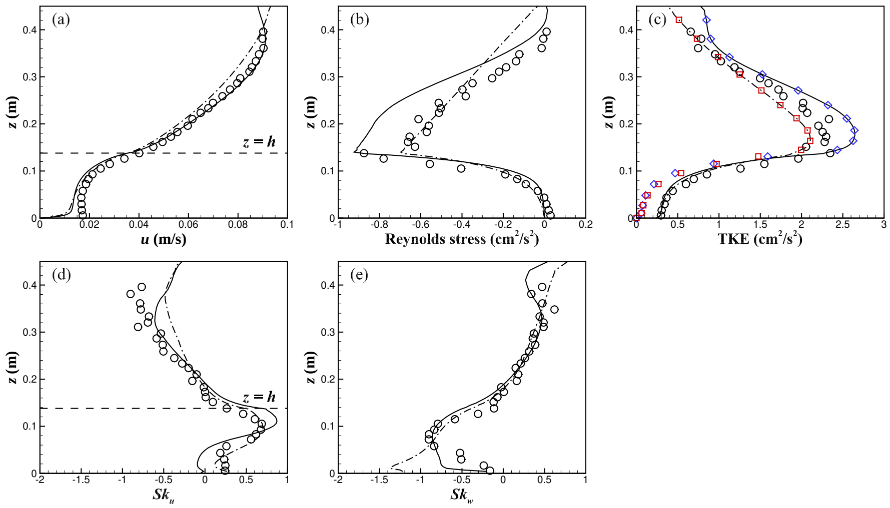

Fig. 2 Vertical profiles of time and lateral averaged velocity and turbulence statistics (a) Streamwise velocity; (b) Reynolds stress; (c) Turbulence kinetic energy (TKE) with the stem-scale TKE Eq.(5) included; (d) Skewness of streamwise velocity; (e) Skewness of vertical velocity. Solid and dashed lines respectively represent simulations with no-slip sidewall and spanwise-periodic conditions. Opened circles from Ghisalberti's flume measurement. In the subfigure 2c, opened diamonds and opened squares represent the computed TKE without the stem-scale TKE Eq.(5) included under sidewall condition and periodic lateral condition respectively.

illustrate the contribution of the stem-scale TKE, the computed TKE from both simulations without the addition of Eq.(5) have also been included in Fig. 2c. According to our calculation, the stem-wake turbulence from Eq.(5) contributed approximately 36% of the total TKE in the lower canopy.

3.2 Coherent Structures

Coherent structures play a central role in the vertical turbulent transfer of mass and momentum between the canopy and overflow [13,31]. Hence, a proper characaterization of coherent structures is important in modeling canopy flows.

3.2.1 Quadrant analysis

Quadrant analysis has been used to describe the structure of coherent structures in canopy flows (see Finnigan [36]), and it is used here to explore whether the LES appropriately captured the impact of coherent structures on momentum transport. Quadrant analysis (QA) categorizes the instantaneous Reynolds stress ($u'w'$) into four quadrants [37]:

– Quadrant 1 (Q1): outward interaction ($u' > 0$ and $w' > 0$)
– Quadrant 2 (Q2): ejection ($u' < 0$ and $w' > 0$)

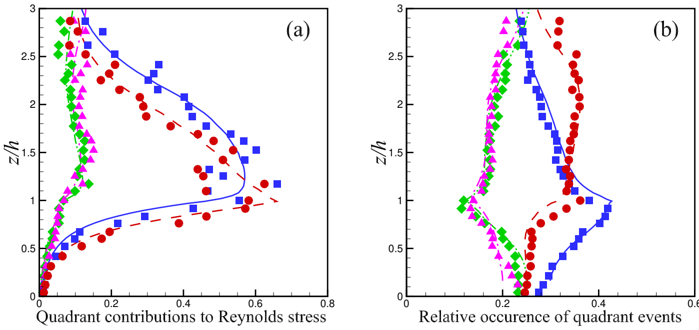

Fig. 3 Vertical distributions of (a) the contribution of each of the four quadrants to Reynolds stress, and (b) the relative frequency of events in each quadrant. Dashed double dotted line (Q1), solid line (Q2), dashed dotted line (Q3), and dashed line (Q4) from LES with no-slip sidewalls; filled diamonds (Q1), filled squares (Q2), filled triangles (Q3), and filled circles (Q4) from the experiment of Ghisalberti and Nepf [31].

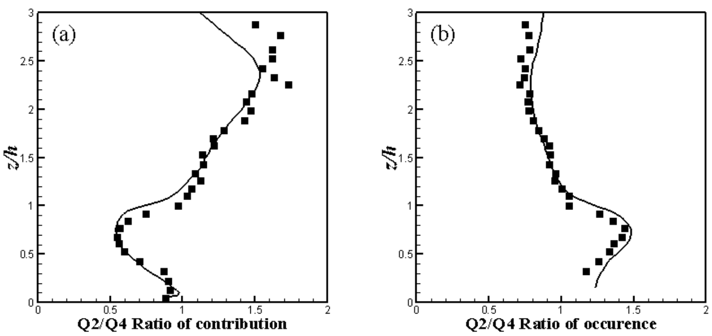

Fig. 4 (a) Ratio of contributions to Reynolds shear stress from Q2 events to that from Q4 events; (b) Ratio of number of Q2 events to that of Q4 events. Solid line, present LES; squares, experiment of Ghisalberti and Nepf [31].

– Quadrant 3 (Q3): inward interaction ($u' < 0$ and $w' < 0$)
– Quadrant 4 (Q4): sweep ($u' > 0$ and $w' < 0$)

The absolute value of the contribution to momentum flux made by the Qth quadrant $\left|\overline{u'w'}_Q/\overline{u'w'}\right|$ is shown in Fig. 3a, which compares the simulated values (solid lines) with the experimental data (R8 in Ghisalberti and Nepf [31], shown with solid symbols). The simulation produced good agreement with measurements both within and above the canopy layer. The model also reproduced the relative frequency of each event type (Fig. 3b). From these two figures, we can see that in the upper canopy and extending to the water surface, Q2 ejection events and Q4 sweep events were the dominant contributors to turbulent momentum transfer. Figure 3 shows that the turbulent momentum flux did not penetrate to the bed, which is consistent with the high canopy density ($ah = 1.1$). Both figures confirm that the LES correctly captured the influence of the coherent structures on the turbulence field.

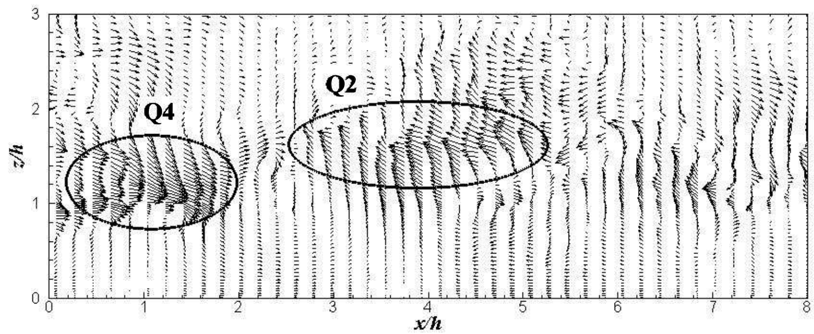

Fig. 5 Instantaneous snapshot of the fluctuating component of the velocity vector of (u', w') in an (x, z) plane along the centerline of the vegetated channel. A sweep event (Q4) and ejection event (Q2) are circled and labeled.

Figure 4 depicts the ratio of contributions to Reynolds shear stress from Q2 events to that from Q4 events and their frequency of occurrence, which were found to collapse with the experimental measurements of Ghisalberti and Nepf [31]. Within the upper canopy layer, the less frequent sweep events contribute more to momentum transfer than ejection events, whereas the opposite situation occurs from the canopy interface up to the free surface.

Figure 5 displays an instantaneous snapshot of the fluctuating velocity vector of (u', w') in an (x, z) plane along the centerline of the vegetated channel, from which we can observe that alternating Q2 (ejection) events and Q4 (sweep) events were the dominant forms of coherent structures at and just above the canopy interface ($z/h = 1$). The coherent motions reached almost to the water surface, but decayed rapidly with distance into the canopy, making little contribution below $z/h = 0.6$ (based on the average of several instantaneous snapshots). Similarly, the Reynolds stress profile (Fig. 2b and 3a), shows that turbulent stress decayed quickly toward zero below $z/h = 0.6$, reflecting the limited sweep penetration into the canopy. The penetration of individual structures (Fig. 5) and their impact on Reynolds stress (Fig. 2) were both consistent with the penetration scale $\delta_e/h = 0.23/C_D ah = 0.4$ (e.g. Nepf et al. [38]), which predicts the distance from the top of the canopy to which the shear-layer coherent structures can penetrate.

3.2.2 Two-point velocity correlation analysis

Two-point velocity correlation analysis was performed to explore the spatial characteristics of the canopy-scale coherent structures. The zero-time-lag, two-point space correlations of the velocity fluctuation components are defined as,

$$R_{ij}(x - L_x/2, y, z, z_{ref}) = \frac{\overline{u'_i(x, y, z)u'_j(0.0, z_{ref})}}{\overline{u'^2_i(x, y, z)}^{1/2}\,\overline{u'^2_j(0, 0, z_{ref})}^{1/2}} \quad (12)$$

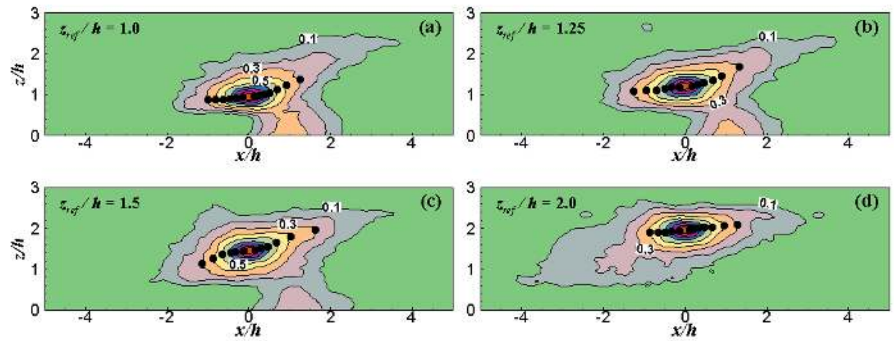

Fig. 6 Contours of streamwise velocity autocorrelations R_{11} in the longitudinal centerplane, with reference points varying in the vertical direction (a) $z_{ref}/h = 1.0$; (b) $z_{ref}/h = 1.25$; (c) $z_{ref}/h = 1.5$; (d) $z_{ref}/h = 2.0$. The black dots represent the locus farthest away from the maximum correlation at each contour level of R_{11} from 0.3 to 1.0.

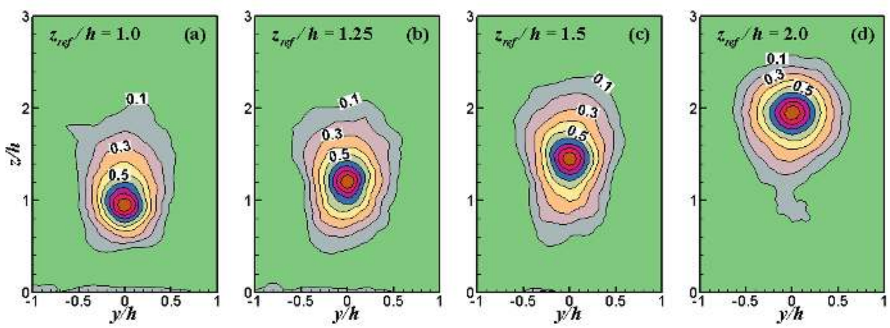

Fig. 7 Contours of streamwise velocity autocorrelations R_{11} in the $y-z$ cross-section. See the caption of Fig. 6.

in which L_x denotes the streamwise length of the computational domain, and the reference point (0,0,z_{ref}) was located in the middle of the horizontal plane of the computational domain with varying vertical heights z_{ref} ($z_{ref}/h = 1.0$, 1.25, 1.5, 2.0). For clarity, the origin of the coordinate system has been shifted horizontally to the center point of the bottom wall. The correlation tensor R_{ij} is a function of the streamwise separation $(x - L_x/2)$, lateral coordinate y, vertical coordinate z and z_{ref}.

The streamwise autocorrelation R_{11} is a standard indicator characterizing the shape and size of coherent structures. Figures 6 and 7 plot the contours of R_{11} for four different reference heights in the longitudinal $(x-z)$ and cross-channel $(y-z)$ centerplanes of the computational domain, respectively. The streamwise velocity component had a high degree of correlation ($R_{11} > 0.3$) within a tilted elliptical region, indicating the presence of inclined elongated turbulent structures above the canopy (Fig. 6). This structure extended approximately $2.5h$ in the streamwise direction and $1.0h$ in the vertical direction, with an average inclination angle decreasing from 18.9° at z_{ref}/h=1.0 to 5.2°

at z_{ref}/h=2.0, as shown in Fig. 6. The angle of inclination was determined by a least-squares method using the points farthest away from the maximum correlation at each contour level from 0.3 to 1.0 [39]. As the reference height increased, the streamwise correlation length associated with $R_{11} = 0.3$ first increased, but then decreased after a certain height between 1.5h and 2.0h. In the channel cross-section $(y - z)$, the strongly correlated region of R_{11} was concentrated in a roughly circular area around $y = 0$ with a lateral extent of h (Fig. 7), which was less than the channel width. This is consistent with Ghisalberti and Nepf [13], who observed multiple structures across the channel of lateral scale comparable to the canopy height h.

The shape of the inclined structure is consistent with that observed in terrestrial canopies [36], but the size in the aquatic canopy modeled here is smaller in the vertical and streamwise directions, which is mostly likely due to the free surface constraining the scale and orientation of coherent structures. Specifically, for a terrestrial canopy, Finnigan [36], reported that the streamwise, lateral and vertical extents of this strongly-correlated region ($R_{11} > 0.3$) are roughly 6h, h and 3h respectively.

3.3 Secondary Circulation

Flow in rectangular channels produces turbulence-induced secondary circulation [40], which has a notable influence on the transport of momentum and mass [41]. Figure 8 shows the contours of the streamwise velocity averaged both temporally and in the streamwise dimension. The magnitude of the lateral and vertical velocity (not shown) was an order of magnitude smaller than the streamwise velocity. The secondary circulation that developed in the vegetated channel with no-slip sidewalls is visualized by the streamlines shown in Fig. 9a. Four large and two small secondary cells were distributed symmetrically across the centerline. For comparison, the streamlines computed in the same channel without vegetation are shown in Fig. 9b, which shows that the presence of submerged vegetation modified the distribution of the secondary cells. Unlike the unvegetated channel (Fig. 9b), no vortices were detected close to the lower corners of the vegetated channel, indicating vegetation drag damped these corner cells.

The secondary circulation transports momentum and thus distorts the contours of streamwise velocity. For example, the upward flow at the centerline and near the bed (Fig. 9a) brings lower velocity upward, bowing the contours of $u = 0.01$ m s^{-1} and 0.02 m s^{-1} upward at the center of the channel (Fig. 8). Near the free surface, circulation carries fluid downward at mid-channel (Fig. 9a), so that the streamwise velocity attains its maximum value below the surface (Fig. 8). It is important to note that these secondary motions do not occur in the spanwise-periodic channel flow (data not shown). Because the LES with no-slip sidewalls correctly captures the secondary flow, it can also reproduce the lateral variation in velocity and turbulence measured in the real channel (Fig. 10). The simulation using the no-slip sidewalls is in reasonable

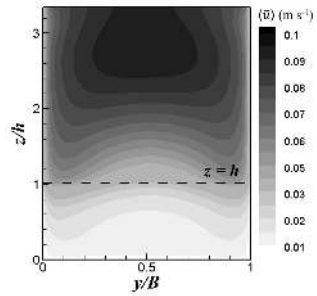

Fig. 8 Contours of mean streamwise velocity $\langle\overline{u}\rangle$ in the $y - z$ plane.

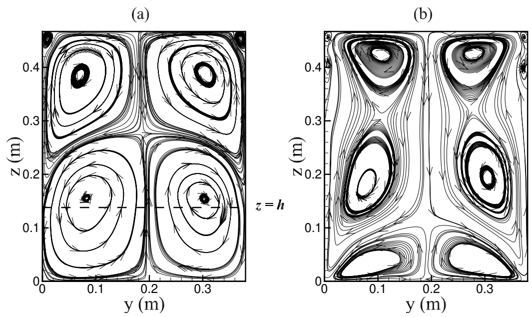

Fig. 9 Secondary flow streamlines computed from LES with no-slip sidewalls in (a) the vegetated open-channel (Table 1); (b) a smooth open-channel with the same dimensions.

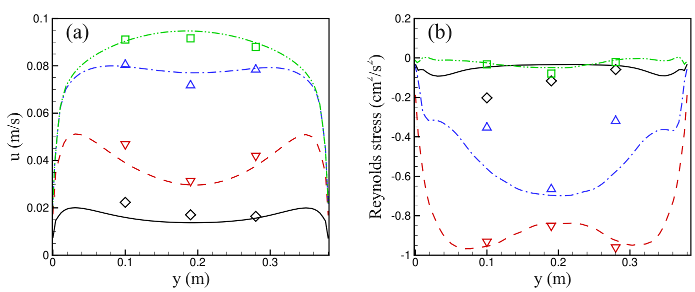

Fig. 10 Lateral profiles of mean flow and turbulence statistics at four different heights $z/h = 0.5$, 1.0, 2.0, 3.0. (a) Mean streamwise velocity; (b) Reynolds stress. Solid line ($0.5h$), dashed line ($1.0h$), dashed dotted line ($2.0h$), and dashed double dotted line ($3.0h$) from LES with no-slip sidewalls; diamonds (0.5h), triangles down (1.0h), triangles up (2.0h), squares (3.0h) from Ghisalberti's flume measurement.

agreement with flume data provided by Ghisalberti (personal communication) from the experiment described in Ghisalberti and Nepf [13]. In the lower part of the channel, specifically $z/h \leq 2.0$ [diamonds and triangles], the streamwise velocity (u) has its maximum value near the side walls, while at $z/h = 3.0$ [squares], u peaks in the center (Fig. 10a). These variations can be attributed

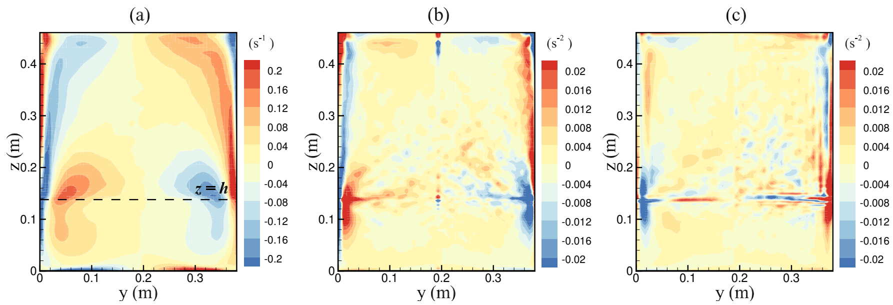

Fig. 11 Contours of (a) mean streamwise vorticity; (b) production by normal stress differences (the second term on the RHS of Eq. 14); (c) production by secondary shear stress (the third term on the RHS of Eq. 14).

to the presence of secondary flow in the cross-plane, as described above. Similarly, the LES with no-slip sidewalls correctly captures the lateral variations in Reynolds stress (Fig. 10b).

The formation of the secondary flow can be understood through the mean streamwise vorticity [41–43]:

$$\langle \overline{\omega_x} \rangle = \partial \langle \overline{w} \rangle / \partial y - \partial \langle \overline{v} \rangle / \partial z \tag{13}$$

The equation for $\langle \overline{\omega_x} \rangle$ is derived from the vertical and spanwise momentum equation by eliminating the pressure term,

$$\begin{aligned} \langle \overline{v} \rangle \frac{\partial \langle \overline{\omega_x} \rangle}{\partial y} + \langle \overline{w} \rangle \frac{\partial \langle \overline{\omega_x} \rangle}{\partial z} =& \upsilon \left(\frac{\partial^2}{\partial y^2} + \frac{\partial^2}{\partial z^2} \right) \langle \overline{\omega_x} \rangle + \frac{\partial^2}{\partial y \partial z} \left(\left\langle \overline{v'^2} \right\rangle - \left\langle \overline{w'^2} \right\rangle \right) \\ &+ \left(\frac{\partial^2}{\partial z^2} - \frac{\partial^2}{\partial y^2} \right) \left\langle \overline{v'w'} \right\rangle + \frac{\partial^2}{\partial y \partial z} \left(\langle \overline{v}''^2 \rangle - \langle \overline{w}''^2 \rangle \right) \\ &+ \left(\frac{\partial^2}{\partial z^2} - \frac{\partial^2}{\partial y^2} \right) \langle \overline{v}'' \overline{w}'' \rangle + \left(\frac{\partial \left\langle \overline{F_{Dy}} \right\rangle}{\partial z} - \frac{\partial \left\langle \overline{F_{Dz}} \right\rangle}{\partial y} \right) \end{aligned} \tag{14}$$

The two terms on the left-hand-side (LHS) represent the convection of streamwise vorticity, and the first term on the right-hand-side (RHS) stands for the viscous diffusion of streamwise vorticity. The remaining terms generate or dampen the secondary circulation. Given that the ratio of the flume width to the diameter of the cylinder is approximately 60, the stem-scale structures in the wake of each vegetation element were assumed to have a minor effect upon the flume-width-scale secondary structures.

The secondary flow above the canopy layer was generated only by turbulent stress fluctuations, i.e. the normal stress differences $\left\langle \overline{v'^2} \right\rangle - \left\langle \overline{w'^2} \right\rangle$ and the secondary shear stress $\left\langle \overline{v'w'} \right\rangle$. The contours of mean streamwise vorticity and the production terms associated with the normal stress differences and secondary shear stress all display an antisymmetric distribution about the channel centerline (Fig. 11a-c). The vorticity $\langle \overline{\omega_x} \rangle$, was mainly produced

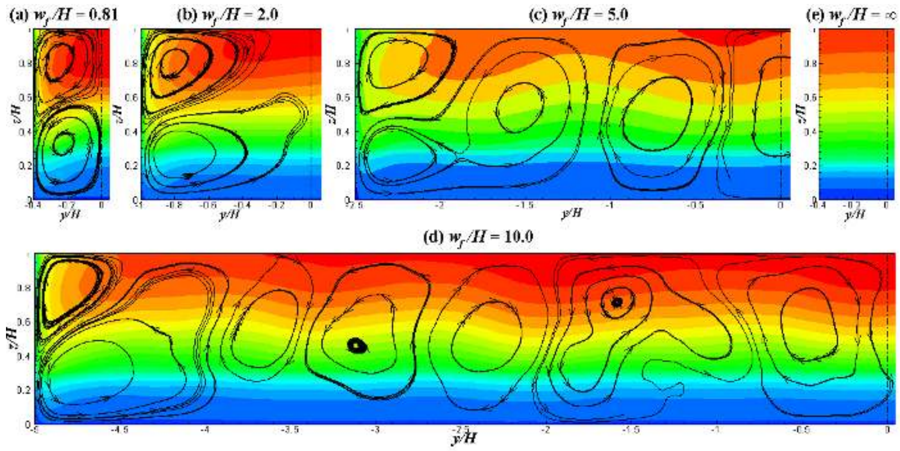

Fig. 12 LES computed secondary flow streamlines along with contours of mean streamwise velocity for all cases. Note that only half of the channel width is shown, with y/H=0 at the centerline.

along the sidewalls between the top of the canopy to the upper corner, with an intense region of production coincident with the top of the canopy (Fig. 11). This implies that the canopy height controlled the position of the secondary circulation. In addition, the distribution of $\langle \overline{\omega_x} \rangle$ was positively correlated with the production term associated with normal stress differences, and negatively correlated with the production term associated with secondary shear stress, except near the water surface where the opposite correlation exists. This indicates that the secondary shear stress generated the streamwise vorticity near the free surface, while the normal stress differences were the main contribution to vorticity generation in the rest of the channel, and specifically near the top of the canopy, where the canopy roughness and shear-layer were the source of local turbulence intensity driving the gradients in normal stress. Within the canopy layer, dispersive normal stress differences $\langle \overline{v}''^2 \rangle - \langle \overline{w}''^2 \rangle$ and dispersive shear stress $\langle \overline{v}'' \overline{w}'' \rangle$, arise from spatial variation in the time-averaged velocity. However, since the canopy was represented as a distributed drag in the LES simulation, these dispersive terms were absent in the model and thus cannot be the source of secondary circulation within the simulation. The last term on the RHS serves as a destruction term associated with the streamwise component of the curl of vegetation drag vector that acts to inhibits the formation of secondary circulations at the lower corners, as seen in Fig. 9.

The channel aspect ratio has a significant influence on the structure of the secondary flow. Figure 12 depicts the secondary flow streamlines for all simulated cases. For the narrowest channel, the corner vortices filled the channel half-width, with vortex width roughly equal to $0.4h$. In this case, the vortex width is constrained by the channel width. In all other channels of finite width, the upper corner vortex was between $0.5h$ and $0.6h$, irrespective of the aspect ratio (Fig. 12b, c and d). In addition, for the wider channels (w_f/H

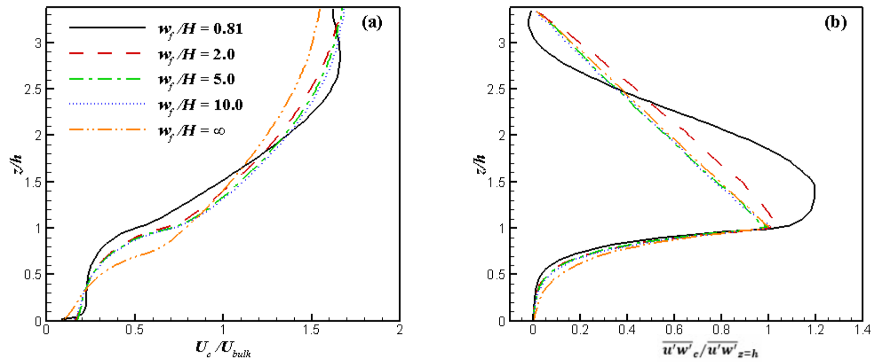

Fig. 13 Vertical profiles of (a) channel centerline velocity U_c and (b) channel centerline Reynolds stress $\overline{u'w'}_c$. The velocity was normalized by the cross-sectionally averaged velocity, U_{bulk}. The Reynolds stress was normalized by its value at the canopy top. The vertical distance z is normalized by the canopy height h.

= 5 and 10), multiple secondary circulation cells appeared across the channel. The width of these secondary cells was roughly equal to H. This multicellular secondary-current flow pattern was consistent with that observed in wide open-channel flows (e.g. Nezu et al. [44] and Culbertson [45]). Note that no secondary motions occurred in the spanwise-periodic channel flow (Fig. 12e).

The impact of the secondary circulations on the streamwise velocity was diminished as the channel aspect ratio increased and the ratio of circulation length-scale to channel width decreased. Specifically, the impact on the time-averaged centerline velocity is shown in Fig. 13a. For the narrowest channel (solid black curve), the maximum centerline velocity occurred below the water surface, which is a classic signature of the impact of secondary circulation on velocity distribution. However, as the channel widened, this feature disappeared, and the maximum centerline velocity occurred at the water surface for all channels wider than $w_f/H \geq 2$. In addition, the change in secondary circulation also impacted the velocity in the upper canopy ($z/h = 0.5$ to 1). Specifically, the streamwise velocity in the upper canopy was the highest for the infinitely wide canopy ($w_f/H = \infty$) where no secondary circulations were present, and the streamwise velocity was the lowest for $w_f/H = 0.81$, where the secondary circulations had the strongest impact. For the $w_f/H = 10$ channel, the secondary circulation was directed downward at the centerline, which could have enhanced velocity in the upper canopy, but, in fact the velocity in the upper canopy was identical to the $w_f/H = 2$ and 5, where the secondary circulations were directed upward and neutral at the centerline, respectively. This comparison suggests that the secondary circulation was not directly responsible for the upper canopy velocity. Instead, the upper canopy velocity was determined by the turbulent momentum flux at the top of the canopy, which was dominated by the coherent structures identified in Fig. 6 and Fig. 7. The lower velocity in the upper canopy for the channels with secondary circulation suggests that the secondary circulations can interfere with the shear-layer coherent structures, making them less effective in vertical momentum exchange. The profiles of Reynolds stress support this interpretation, because the channel without the secondary circulations exhibited the largest penetration of Reynolds stress into the canopy (Fig. 13b).

3.4 Scalar Transport

Figure 14 compares the simulated and measured vertical profiles of mean scalar concentration at six streamwise positions. The concentration has been averaged over the lateral direction and is normalized by the maximum concentration at location 1. The solid and dashed lines respectively represent LES simulations with and without the stem-wake turbulent diffusivity (Eq. 6). The inclusion of the stem-wake diffusivity yielded better agreement with the experimental data of Ghisalberti and Nepf [13], especially near the bed and in the near field (see Fig. 14a), which demonstrates the importance of including the contribution of the unresolved stem-scale turbulence for scalar transport modeling. In the far field, the computed concentration became less sensitive to the inclusion of the stem-wake diffusion model. In the near field, before the plume spreads over the flow depth, the near-bed turbulent diffusion was dominated by stem-scale turbulence, whereas the transport of scalar in the far field (once the plume has spread over the flow depth) was determined by the LES resolved coherent structures.

3.4.1 Characteristics of scalar dispersion plume

The vertical growth rate of the laterally-averaged concentration plume can be quantified by two dispersion parameters, i.e. the mean height of the plume z_m,

$$z_m(x) = \frac{\int_0^H z \left\langle \overline{C} \right\rangle_y (x,z)\mathrm{d}z}{\int_0^H \left\langle \overline{C} \right\rangle_y (x,z)\mathrm{d}z} \tag{15}$$

and its standard deviation in the vertical direction σ_z,

$$\sigma_z(x) = \frac{\int_0^H (z - z_m)^2 \left\langle \overline{C} \right\rangle_y (x,z)\mathrm{d}z}{\int_0^H \left\langle \overline{C} \right\rangle_y (x,z)\mathrm{d}z} \tag{16}$$

The angle bracket with a subscript y indicates a laterally-averaging operation. Because we considered a continuous release, these parameters are only functions of distance x from the source and not of time. Figure 15 plots the streamwise variations of z_m and σ_z, normalized by the canopy height h. The numerical simulations were consistent with the flume measurements. Between the source and $x/h = 5$, z_m was approximately constant, as expected for a plume evolving without influence from any boundaries. Beyond this point, after the plume had reached the no-flux boundary at the bed, z_m increased

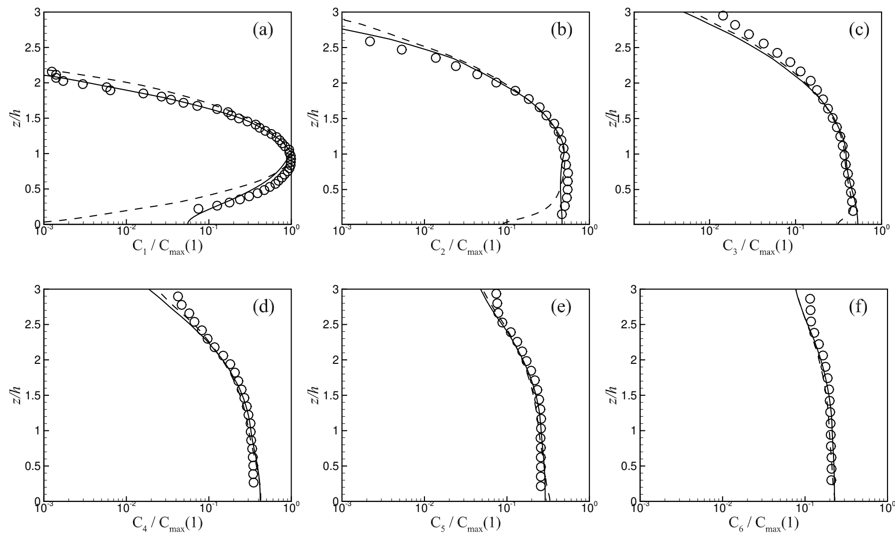

Fig. 14 Comparison of normalized mean concentration profiles from LES simulation and experimental data. (a) x = 19 cm; (b) x = 54 cm; (c) x = 92 cm; (d) x = 150 cm; (e) x = 250 cm; (f) x = 380 cm. Solid and dashed lines, respectively, indicate simulation results obtained with and without turbulent diffusivity model (Eq. 6). Symbols are experimental measurements [13].

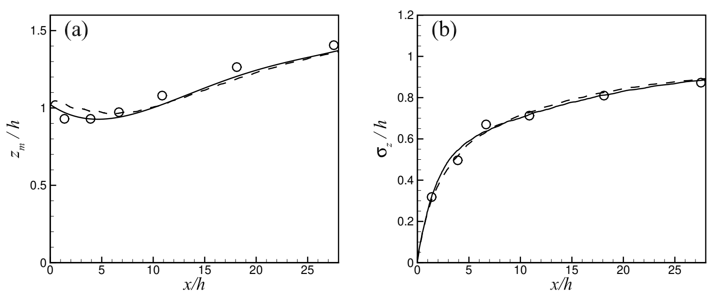

Fig. 15 Comparisons of streamwise variations of (a) z_m/h and (b) σ_z/h between LES results and experimental data. For legend, see caption of Fig. 14.

with x. The LES with stem-wake diffusivity matched the data more closely in the near-field ($x/h < 5$), but in the far field, the models with and without stem-wake diffusivity converged (Fig. 15), because once the plume scale was comparable to the coherent shear-layer structures and the secondary circulation cells (e.g. Fig. 5), these large structures dominate the scalar transport. Both models provide good predictions of σ_z (Fig. 15b).

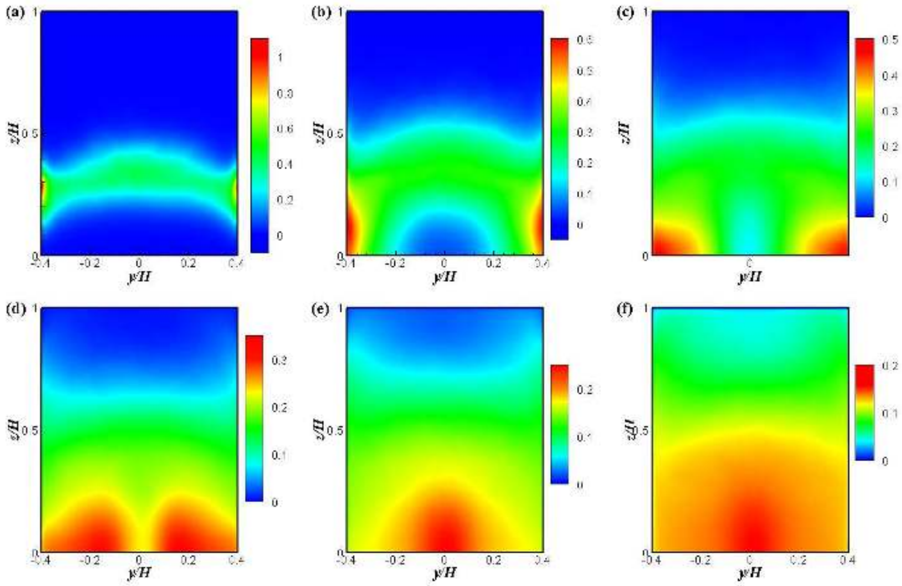

Fig. 16 Contours of normalized, time-mean scalar concentration on six crossplanes along the streamwise direction from (a) to (f): (a) x = 19 cm; (b) x = 54 cm; (c) x = 92 cm; (d) x = 150 cm; (e) x = 250 cm; (f) x = 380 cm. The vertical and lateral coordinates are normalized by the water depth H.

3.4.2 Effects of secondary flow on scalar dispersion

Secondary circulations can be an important mechanism of scalar transport in fluvial systems [21]. Similarly, the secondary circulation within the vegetated channel impacted the distribution and mixing of scalar. Figure 16 plots the contours of time-averaged concentration at six crossplanes along the streamwise direction for the original channel ($w_f/H = 0.81$). The location of the concentration maxima moved with the secondary circulation. Although the scalar was discharged from sources uniformly distributed in the lateral direction, the secondary circulation distorted the tracer distribution. At the top of the canopy, the vertical velocity associated with the secondary circulation was upward at the channel centerline and downward near the walls. This caused the maximum concentration to be deflected upward at the centerline and downward at the walls. This distortion is clearly seen in the concentration contours near the source (Fig. 16a). Farther from the source, the advection of tracer associated with the secondary circulation within the canopy (Fig. 8b and c) produced maximum concentrations at the bottom corners (Fig. 16b and c), and eventually the maximum concentration was advected to the center at the bed (Fig. 16d). That is, the maximum concentration within the canopy traced out the trajectory imposed by the secondary circulation. Similarly, as the tracer entered the pair of cells above the canopy, the contours of scalar concentration were bent upward at the sidewalls by the secondary circulation in this region.

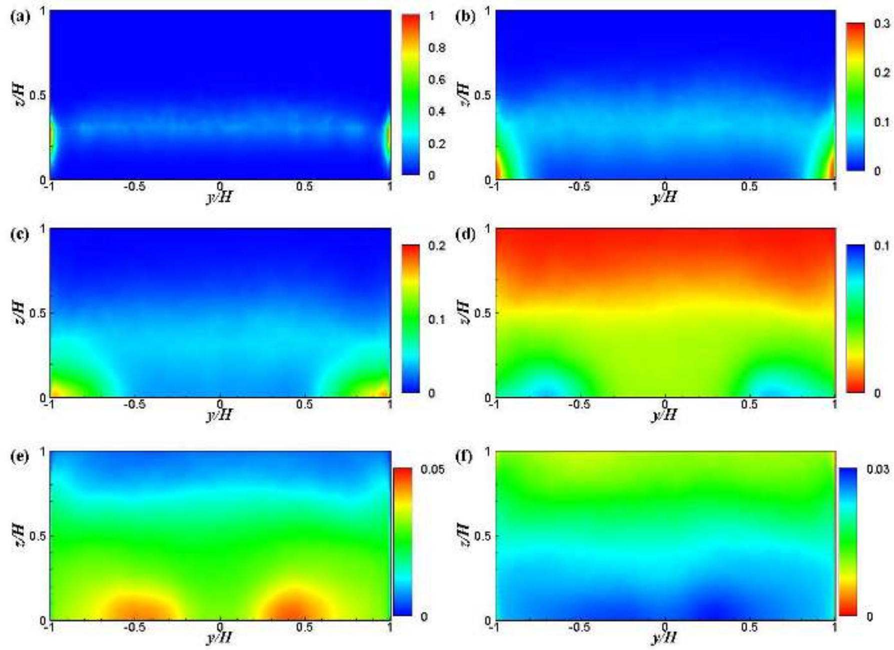

Fig. 17 Contours of normalized, time-mean scalar concentration on six crossplanes along the streamwise direction of the channel of $w_f/H = 2.0$. See the caption of 16.

3.4.3 Effects of the channel aspect ratio

As the channel aspect ratio w_f/H increased, the number of secondary circulation across the channel also increased, with neighboring cells rotating in opposite directions (Fig. 12). The presence of multiple secondary circulations enhanced the scalar mixing within the central zone of the open-channel, while near the sidewalls, the scalar was transported in a manner similar to the validated case, i.e. the corner secondary cells advected the maximum concentration from the canopy interface to the lower corners (Fig. 17). For the spanwise periodic channel, there are no secondary cells to distort the evolving tracer cloud, and the scalar plume spreads vertically in a uniform fashion across theNote that to represent the infinitely wide channel, the side boundaries were assigned convective boundary conditions for the scalar modeling, which allowed the scalar to leave the observed domain. As a result, the scalar distribution is non-uniform in the lateral direction. channel (see Fig. 18).

Figure 19 shows the vertical profiles of laterally-averaged concentration from simulated cases with different channel aspect ratios, normalized by the average value of the cross-section at each downstream location. The vertical spread of the tracer plume was the slowest for the spanwise periodic channel (dashed-dot curve in Fig. 19) which contained no secondary circulations, indicating that the secondary circulation enhanced the vertical transport of scalar in the other channels. In the near field, the narrowest channel exhibited the

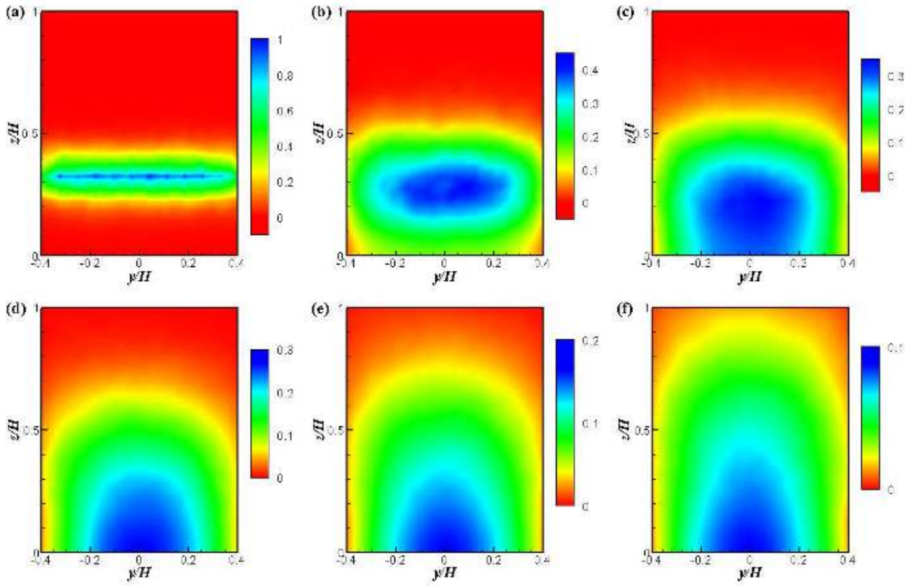

Fig. 18 Contours of normalized, time-mean scalar concentration on six crossplanes along the streamwise direction for the spanwise periodic channel. See the caption of 16.

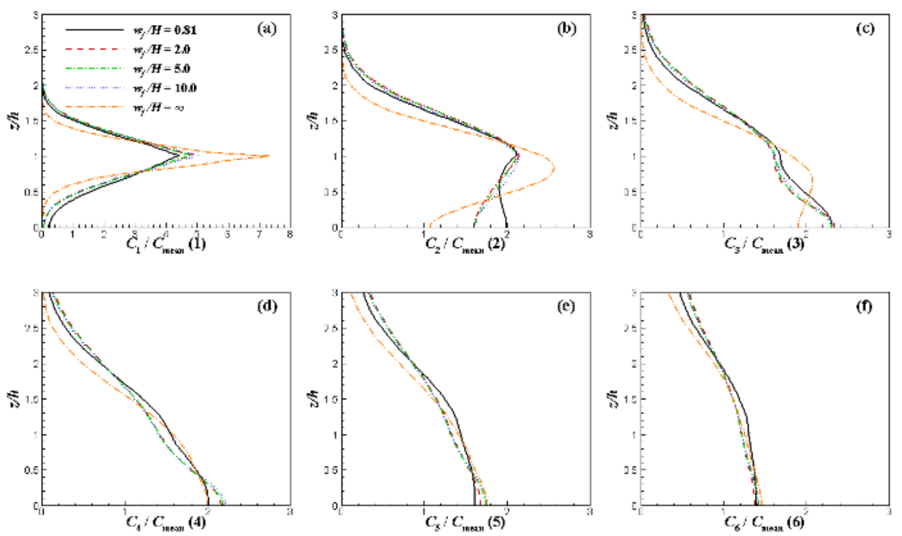

Fig. 19 Comparison of normalized, time-mean concentration profiles for simulated cases with different channel aspect ratios. (a) x = 19 cm; (b) x = 54 cm; (c) x = 92 cm; (d) x = 150 cm; (e) x = 250 cm; (f) x = 380 cm.

fastest vertical spread of tracer, because the corner vortices extended across the channel, efficiently enhancing the scalar transport within the canopy layer. In the far field, once the plume had reached the bed, the concentration profiles for all open-channels collapsed with each other at all downstream locations.

Finally, also note that the secondary cells particularly enhanced the downward spread of tracer into the canopy. For example, Fig. 19b shows that the tracer spread downward much faster within the channels of finite width. In addition, the narrowest channel (solid line in Fig. 19b) developed a secondary concentration peak within the canopy. This feature is non-Fickian, and can be attributed to the fact that the secondary structures controlling the vertical migration of tracer were comparable in size to the plume, creating what appeared to be counter-gradient fluxes and generating a local peak below the injection site.

4 Conclusion

In this paper, LES was used to predict the turbulence structure and the transport of a passive scalar in an open channel with submerged vegetation. For simplicity, the vegetation was represented by a distributed drag force proportional to the canopy density and local, resolved velocity. In the scalar transport equation, the effect of stem-scale eddies, which were not directly resolved by the LES, was introduced by adding the scalar diffusivity model proposed and validated by Tanino and Nepf [18]. The model performance was evaluated by comparing the simulation to flume data from Ghisalberti and Nepf [13]. Satisfactory agreements were found between LES and measurements of turbulence statistics and mean concentration, which demonstrated that the LES correctly captured the coherent structures formed at the canopy interface and their impact on momentum and scalar transport. Importantly, the inclusion of stem-wake TKE and diffusivity was required to match the TKE levels and turbulent scalar transport in the lower canopy layer. By extension, the LES model presented here applies equally to mass transport within and above terrestrial plant canopies.

Quadrant analysis and instantaneous velocity maps showed that Q2 ejection events and Q4 sweep events were the dominant types of coherent structures within a vegetated channel. Sweeps (Q4) carried most of the momentum flux into the upper canopy layer, whereas ejections (Q2) dominated above the canopy. Statistical space correlation revealed an inclined elongated coherent structure lying above the vegetation canopy, with an extent of $2.5h$, h and h in the streamwise, lateral and vertical directions respectively. The free surface and side walls affected the extension and orientation of this structure, as the size and inclination angle were smaller than that observed in terrestrial vegetation canopies.

The study also revealed important shifts in the secondary circulation commonly found in the open channel flow. In the channel of narrow aspect ratio ($w_f/H = 0.81$), the vegetated channel produced a secondary flow structure composed of four counter-rotating vortices and two corner vortices, which differed from the well-known eight-vortex pattern observed in a square duct bounded by four solid walls. The position of the secondary cells was linked to the canopy height, because the elevated turbulence intensity at the top of the canopy provokes the generation of streamwise vorticity via gradients in the normal turbulent stresses. Importantly, the secondary flow was shown to cause lateral and vertical transport of the scalar plume, which enhanced the vertical mass flux within the vegetated channel.

References

1. Wilcock R, Champion P, Nagels J, Crocker G (1999) The influence of aquatic macrophytes on the hydraulic and physico-chemical properties of a New Zealand lowland stream. Hydrobiologia 416:203–214
2. Schulz M, Kozerski H, Pluntke T, Rinke K (2003) The influence of macrophytes on sedimentation and nutrient retention in the lower River Spree (Germany). Water Res 37:569–578
3. Sand-Jensen K (1998) Influence of submerged macrophytes on sediment composition and near-bed flow in lowland streams. Freshwater Biol 39:663–679
4. Duarte CM, Losada IJ, Hendriks IE, Mazarrasa I, Marbà M (2013) The role of coastal plant communities for climate change mitigation and adaptation. Nat Clim Change 3:961–968
5. Peterson CH, Summerson HC, Duncan PB (1984) The influence of seagrass cover on population structure and individual growth rate of a suspensionfeeding bivalve, Mercenaria mercenaria. J Mar Res 42:123–138
6. Irlandi EA, Peterson CH (1991) Modification of animal habitat by large plants: Mechanisms by which seagrasses influence clam growth. Oecologia 87:307–318
7. van Katwijk MM et al (2016) Global analysis of seagrass restoration: the importance of large-scale planting. J Appl Ecol 53:567–578
8. Hughes AR, Stachowicz JJ (2004) Genetic diversity enhances the resistance of a seagrass ecosystem to disturbance. Proc Natl Acad Sci 101:8998–9002
9. Ackerman JD (2002) Diffusivity in a marine macrophyte canopy: implications for submarine pollination and dispersal. Am J Bot 89:1119–1127
10. Murphy E, Ghisalberti M, Nepf HM (2007) Model and laboratory study of dispersion in flows with submerged vegetation. Water Resour Res 43:W05438
11. Lightbody AF, Nepf HM (2006) Prediction of near-field shear dispersion in an emergent canopy with heterogeneous morphology. Environ Fluid Mech 6:477–488
12. Poggi D, Porporato A, Ridolfi L, Albertson JD, Katul GG (2004) The effect of vegetation density on canopy sub-layer turbulence. Boundary-Layer Meteorol 111:565–587
13. Ghisalberti M, Nepf HM (2005) Mass transport in vegetated shear flows. Environ Fluid Mech 5:527–551
14. Ghisalberti M, Nepf HM (2004) The limited growth of vegetated shear layers. Water Resour Res 40:W07502
15. Raupach MR, Finnigan JJ, Brunet Y (1996) Coherent eddies and turbulence in vegetation canopies: the mixing-layer analogy. Boundary-Layer Meteorol 78:351–382
16. Nepf HM, Vivoni ER (2000) Flow structure in depth-limited, vegetated flow. J Geophys Res: Oceans 105:28547–28557
17. López F, García M (2001). Mean flow and turbulence structure of open-channel flow through non-emergent vegetation. J Hydraul Eng 127:392–402
18. Tanino Y, Nepf HM (2008) Lateral dispersion in random cylinder arrays at high Reynolds number. J Fluid Mech 600:339–371
19. King AT, Tinoco RO, Cowen EA (2012) A $k-\varepsilon$ turbulence model based on the scales of vertical shear and stem wakes valid for emergent and submerged vegetated flows. J Fluid Mech 701:1–39

20. Okamoto T, Nezu I (2010) Large eddy simulation of 3-D flow structure and mass transport in open-channel flows with submerged vegetations. J Hydr Res 4:185–197
21. Chant RJ (2010) Estuarine secondary circulation. In: Valle-Levinson A (eds) Contemporary issues in estuarine physics. Cambridge University press, Cambridge, pp 100–124
22. Bradshaw P (1987) Turbulent secondary flows. Annu Rev Fluid Mech 19:53–74
23. Nepf HM, Sullivan JA, Zavistoski RA (1997) A model for diffusion within emergent vegetation. Limnol Oceanogr 42:1735–1745
24. Meneveau C, Lund TS, Cabot WH (1996) A Lagrangian dynamic subgrid-scale model of turbulence. J Fluid Mech 319:353–385
25. Cui J, Neary VS (2008) LES study of turbulent flows with submerged vegetation. J Hydraul Res 46:307-316
26. Yue W, Parlange MB, Meneveau C, Zhu W, Hout R, Katz J (2007) Large-eddy simulation of plant canopy flows using plant-scale representation. Boundary-Layer Meteorol 124:183-203
27. Vinçont JY, Simoëns S, Ayrault M, Wallace JM (2000) Passive scalar dispersion in a turbulent boundary layer from a line source at the wall and downstream of an obstacle. J Fluid Mech 424:127–167
28. Rossi R, Iaccarino G (2009) Numerical simulation of scalar dispersion downstream of a square obstacle using gradient-transport type models. Atmos Environ 43:2518–2531
29. Jansen KM, Kong B, Fox RO, Hill JC, Olsen MG (2015) Large eddy simulation of passive scalar transport in a high Schmidt number turbulent incompressible wake with experimental validation. Chem Eng Sci 137:862–874
30. Yan C, Huang WX, Cui GX, Xu C, Zhang ZS (2015) A ghost-cell immersed boundary method for large-eddy simulation of flows in complex geometries. Int J Comput Fluid Dyn 29:12–25
31. Ghisalberti M, Nepf HM (2006) The structure of the shear layer in flows over rigid and flexible canopies. Environ Fluid Mech 6:277–301
32. Belcher SE, Jerram N, Hunt JCR (2003) Adjustment of a turbulent boundary layer to a canopy of roughness elements. J Fluid Mech 488:369–398
33. Bou-Zeid E, Parlange MB, Meneveau C (2007) On the parameterization of surface roughness at regional scales. J Atmos Sci 64:216–227
34. Cassan L, Belaud G, Baume JP, Dejean C, Moulin F (2015) Velocity profiles in a real vegetated channel. Environ Fluid Mech 15:1263–1279
35. Nezu I, Nakagawa H (1989) Self-forming mechanism of longitudinal sand ridges and troughs. Proc 23rd IAHR Congress Vol B, IAHR, Delft, The Netherlands, 65–72
36. Finnigan JJ (2000) Turbulence in plant canopies. Annu Rev Fluid Mech 32:519–571
37. Wallace JM (2016) Quadrant analysis in turbulence research: history and evolution. Annu Rev Fluid Mech 48:131–158
38. Nepf HM, Ghisalberti M, White B, Murphy E (2007) Retention time and dispersion associated with submerged aquatic canopies. Water Resour Res 43:W04422
39. Volino RJ, Schultz MP, Flack KA (2007) Turbulence structure in rough- and smooth-wall boundary layers. J Fluid Mech 592:263–293
40. Perkins HJ (1970) The formation of streamwise vorticity in turbulent flow. J Fluid Mech 44:721–740
41. Huser A, Biringen S (1993) Direct numerical simulation of turbulent flow in a square duct. J Fluid Mech 257:65–95
42. Gavrilakis S (1992) Numerical simulation of low-Reynolds-number turbulent flow through a straight square duct. J Fluid Mech 244:101–129
43. Ghisalberti M (2010) The three-dimensionality of obstructed shear flows. Environ Fluid Mech 10:329–343
44. Nezu I, Nakagawa H, Tominaga A (1985) Secondary Currents in a Straight Channel Flow and the Relation to Its Aspect Ratio. In: Bradbury LJS, et al. (eds) Turbulent Shear Flows 4. Springer, New York, pp 246–260.
45. Culbertson JK (1967) Evidence of secondary circulation in an alluvial channel. Geological Survey Research, US Geol Survey, D214-D215.